Internal Waves in the Arctic: Influence of Ice Concentration, Ice Roughness, and Surface Layer Stratification

Sylvia T. Cole[1] [iD], **John M. Toole[1]** [iD], **Luc Rainville[2], and Craig M. Lee[2]**

[1]Woods Hole Oceanographic Institution, Woods Hole, MA, USA, [2]Applied Physics Laboratory, University of Washington, Seattle, WA, USA

Abstract The Arctic ice cover influences the generation, propagation, and dissipation of internal waves, which in turn may affect vertical mixing in the ocean interior. The Arctic internal wavefield and its relationship to the ice cover is investigated using observations from Ice-Tethered Profilers with Velocity and Seaglider sampling during the 2014 Marginal Ice Zone experiment in the Canada Basin. Ice roughness, ice concentration, and wind forcing all influenced the daily to seasonal changes in the internal wavefield. Three different ice concentration thresholds appeared to determine the evolution of internal wave spectral energy levels: (1) the initial decrease from 100% ice concentration after which dissipation during the surface reflection was inferred to increase, (2) the transition to 70–80% ice concentration when the local generation of internal waves increased, and (3) the transition to open water that was associated with larger-amplitude internal waves. Ice roughness influenced internal wave properties for ice concentrations greater than approximately 70–80%: smoother ice was associated with reduced local internal wave generation. Richardson numbers were rarely supercritical, consistent with weak vertical mixing under all ice concentrations. On decadal timescales, smoother ice may counteract the effects of lower ice concentration on the internal wavefield complicating future predictions of internal wave activity and vertical mixing.

Plain Language Summary This study addresses how seasonal changes in the Arctic Ocean's floating sea ice influence the ocean's small-scale, high-frequency currents. These motions can influence the distribution of heat and other water properties in the Arctic Ocean but are not resolved in numerical models and so need to be parameterized. Observations from the 2014 Marginal Ice Zone experiment are used to collectively analyze over 8,500 profiles of temperature and salinity, and over 5,000 profiles of velocity in the upper 250 m of the Arctic Ocean's Canada Basin. These observations began in March beneath a contiguous ice sheet; by fall the measurement domain included regions of low ice concentration as well as open water. The ocean's high-frequency currents changed abruptly in response to changes in the ice cover, with the lowest energy observed beneath a fractured ice cover and the largest energy in open water. The under-ice topography also influenced the ocean's high-frequency currents, with smoother topography corresponding to weaker ocean currents. The primary implication is that contrasts between smoother versus rougher under-ice topography and a fractured versus continuous ice cover are critical for understanding the interactions between the ocean and sea ice, now and in the future.

1. Introduction

Internal waves influence velocity shear throughout the water column and thus the vertical turbulent exchanges of heat and momentum and so can potentially influence the Arctic ice cover. Interactions between the ice cover, vertical mixing, and warm waters at depth have long been recognized, with the commonly cited paradigm of persistently low internal wave energy levels and vertical mixing (Fer, 2009; Guthrie et al., 2013; Lincoln et al., 2016) with internal wave shear variance and vertical mixing influenced by ice concentration and/or mixed layer depth (Fer, 2014; Guthrie et al., 2013; Morison et al., 1985; Rainville & Woodgate, 2009; Randelhoff et al., 2017). The specific interactions between the properties of the ice cover (its concentration or roughness) and internal wave generation, propagation, and dissipation are imperfectly understood, making it difficult to predict how the Arctic system may change in the future. The changing ice cover (e.g., decreased summer extent, increased speed, and thinner ice) on decadal timescales necessitates an improved understanding of how the ice cover influences internal waves.

The internal wavefield interacts with the ice cover in several ways, and its response to changes in the ice cover is still being explored. Compared with lower latitudes, the Arctic internal wavefield is weak (D'Asaro
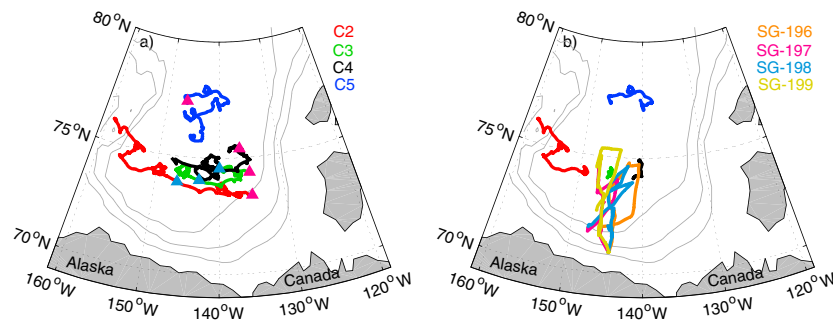
Figure 1. Map of the Canada Basin showing ITP-V drift tracks for C2–C5 (a) spanning March 2014 to December 2014 and (b) during 27 July to 2 October along with locations of the four Seagliders. Gray contours are the 1,000-; 2,000-; and 3,000-m isobaths. Locations of deployment (magenta triangles) and on 23 June (blue triangles) indicated in (a). ITP-V = Ice-Tethered Profiler with Velocity.

& Morehead, 1991; Levine et al., 1985) believed in part due to the ice cover itself and to some extent its location largely above the critical latitude for M2 internal waves (75.06°N) where freely propagating M2 internal waves are precluded (we note that tides have been found to be important near continental slopes; here we focus on the deep interior basins). Internal wave generation has been argued to occur through several mechanisms including wind-driven accelerations of the ice and mixed layer (D'Asaro & Morehead, 1991; Fer, 2014), ice convergences/divergences that locally change mixed layer depth (Halle & Pinkel, 2003), or ice keels that extend into stratified regions (within or beneath the mixed layer; McPhee & Kantha, 1989). The ice cover is also believed to strongly scatter and/or dissipate internal waves during their surface reflection from the under-ice topography (Pinkel, 2005) and limit the horizontal distance internal waves can propagate. For a given region, seasonal contrasts between ice covered and open water areas show that internal wave energy increases in open water conditions (Dosser & Rainville, 2016; Martini et al., 2014), while differences between partial ice concentration and open water appear to be smaller (Randelhoff et al., 2017). Changes to mixed layer depth, whether on seasonal or decadal timescales (e.g., Peralta-Ferriz & Woodgate, 2015), also influence the internal wavefield with shallower mixed layer depths associated with larger internal wave velocities at the surface boundary condition with the ice that results in increased internal wave dissipation (Guthrie et al., 2013; Morison et al., 1985). Taken together, the generation, propagation, and dissipation of internal waves are directly influenced by the wind forcing, ice cover, and ocean stratification.

The goal of this study is to determine the relative influence of ice concentration, ice roughness, and surface layer stratification on the generation, propagation, and dissipation of internal waves and so further understanding of the Arctic vertical mixing paradigm. This is accomplished by analyzing observations that derive from the Office of Naval Research Marginal Ice Zone (MIZ) experiment (Lee et al., 2012) in the Canada Basin that took place throughout the 2014 melt season (Figure 1).

1.1. Relevant Results From the MIZ Experiment

Here we consider observations from four instrument clusters (C2–C5) of the five that were moored into and drifted with the sea ice, along with data from four Seagliders that sampled both open water and MIZ domains (Figure 1). The present study is a companion paper to Cole et al. (2017) which addressed momentum transfer in the air-ice-ocean system at low frequencies (daily averaged motions) utilizing the same data set of ice and ocean currents. The evolution of the ice floe size distribution and thermodynamics of the ice cover and surface layer observed during the MIZ experiment are described by Hwang et al. (2017) and Gallaher et al. (2016), respectively.

Evolution of the ice cover, upper ocean velocity, and surface layer stratification was largely coherent across C2–C4 due to the large scale of the wind forcing and solar heating (Cole et al., 2017; Gallaher et al., 2016). The ice began to break up with initial minor decreases in ice concentration (Figure 2a) due to wind events in late April and early May (Figure 2b). Ice concentrations were similar at C2–C4 through July with similar timing of, for example, melt pond drainage (late June to early July) and mixed layer depth shoaling (mid-July).
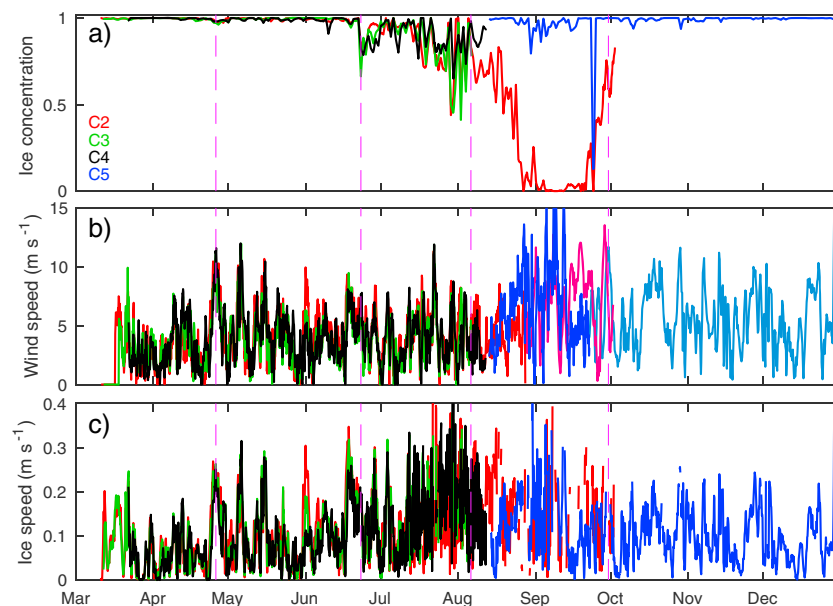
Figure 2. (a) AMSR-2 ice concentration, (b) directly observed wind speed with Era-Interim wind speed at C2 (magenta over 27 August to 2 October) and C5 (light blue over 22 September to 31 December), and (c) directly observed ice speed at the cluster locations. Dashed vertical magenta lines mark 26 April, 23 June, 6 August, and 30 September. Elevated near-inertial motions of the ice manifest as rapid changes in August and September ice velocity. AMSR = Advanced Microwave Scanning Radiometer 2.

The smallest ice concentration was observed at C2 in September (Figure 2a), with ice remaining about C2 throughout the melt season (Figure 7 of Cole et al., 2017).

The ice cover at C2–C4 had different physical under-ice roughness. Median ice-ocean drag coefficients relevant to the subinertial motions, which are estimated from observations of the turbulent momentum flux and ice and 6-m ocean velocities, are summarized in Table 1 (see also Figure 12 of Cole et al., 2017). Ice-ocean drag coefficients were estimated on a daily timescale with significant daily variability resulting from variations in, for example, ice speed or relative direction of the ice-ocean shear (e.g., McPhee, 2012). Here we are interested in the monthly scale variations in drag coefficients that result from dynamic or thermodynamic changes to the ice cover. On this monthly timescale, the ice at C2 was a factor of 3 smoother during March–June due to larger multiyear ice floes embedded within the first-year ice/multiyear ice conglomerate (Cole et al., 2017). The ice-ocean drag coefficient increased at C3 during 15 May to 27 June due to rearrangement of the ice cover (Cole et al., 2017). All estimated ice-ocean drag coefficients were smaller than the canonical value of 5.5×10^{-3} (McPhee, 1980).

2. Data

2.1. Ice-Tethered Profilers With Velocity

Ice-Tethered Profiler with Velocity (ITP-V) systems yield profiles of temperature, salinity, and absolute ocean velocity while moored into and drifting with the supporting ice cover. ITP-Vs were deployed at MIZ instrument clusters 2–5 (C2–C5, Figure 1a) and returned profiles from ~7- to 250-m depth every 3 hr between 10 March to 2 October at C2 (ITP-77), 11 March to 6 August at C3 (ITP-78), 21 March to 12 August at C4 (ITP-79 and one profile per day through 29 September), and 13 August 2014 to 24 May 2015 at C5 (ITP-80). Here we only consider data at C5 through 31 December 2014 and collectively analyze 5,099 profiles. Details of the velocity observations and processing are in Cole et al. (2015) and appendix B of Cole et al. (2017). Conductivity, temperature, and depth data were processed as in Dosser et al. (2014).

Table 1

Median Daily Averaged Ice-Ocean Drag Coefficient at 6-m Depth for Each Cluster and Time Period

Cluster	March to 15 May	15 May to 27 June	1 September to 30 October
C2	1.0×10^{-3}	0.8×10^{-3}	—
C3	2.8×10^{-3}	5.1×10^{-3}	—
C4	3.6×10^{-3}	2.4×10^{-3}	—
C5	—	—	4.4×10^{-3}

Note. See also Figure 12 of Cole et al. (2017).
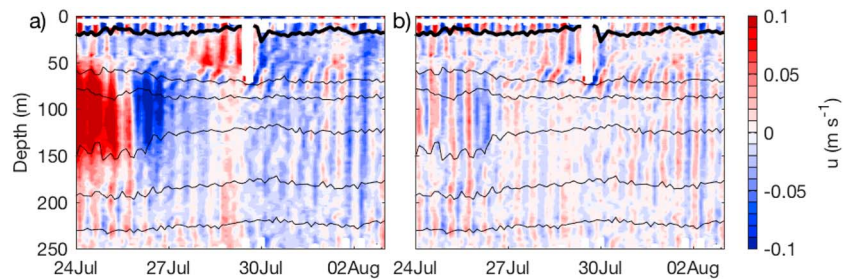
Figure 3. A 10-day segment at C2 during late July of (a) instantaneous eastward velocity and (b) high-pass filtered eastward velocity. Mixed layer depth (thick black lines) and depths of selected isopycnals spaced apart by 0.5 kg/m^3 (thin lines) are shown. Ice velocity is plotted in a band at 0- to 3-m depth. The color scale is saturated with the largest velocities corresponding to closed eddies that had speeds as large as 0.3 m/s.

2.2. Seagliders

Four Seagliders (196-199) operated during the period 27 July to 2 October 2014. The Seagliders deliberately transited from open water to beneath the ice cover and occasionally made short repeat transects across the ice edge (Figure 1b). For most of their mission, the gliders profiled from the surface (or ~1–2 m beneath the ice in the presence of sea ice) to 750-m depth approximately every 3.5 hr. Here we consider the upper ~250-m segments of the temperature and salinity profiles (a total of 3,454 profiles). Seagliders and their data processing are further described in Eriksen et al. (2001).

2.3. Ice Concentration

Satellite-based ice concentration from the Advanced Microwave Scanning Radiometer 2 on a 3.125-km grid (Spreen et al., 2008) was averaged within a 15-km radius of each ITP-V profile location and Seaglider dive location (e.g., Figure 2a). As shown in Cole et al. (2017), targeted high-resolution visual remote sensing observations about the instrument clusters showed good agreement with Advanced Microwave Scanning Radiometer 2 values, with the exception of September when targeted images showed higher ice concentrations and confirmed that ice remained about the buoy clusters throughout the melt season (see Figure 7 of Cole et al., 2017).

2.4. Wind Velocity

Directly observed and European Center for Medium-Range Weather Forecasts ERA-Interim (ERA-I) wind velocity estimates are utilized (e.g., Figure 2b). Wind velocity was measured from Autonomous Weather Stations at the center of each instrument cluster (C2–C5) every 15 min (see Cole et al., 2017). ERA-I wind velocity was utilized at C2 after 27 August and at C5 after 22 September when direct wind observations were not available and in the analysis of all Seaglider profiles. When both directly observed and ERA-I winds were compared (both interpolated to the times of ITP-V profiles), their correlation was high (e.g., $r^2 = 0.88$ with a slope of 1.02 for wind speed at C2 during 16 March to 26 August; not shown).

3. Methods

3.1. Instantaneous Profiles

Mixed layer depth was estimated for each ITP-V or Seaglider profile using a density difference threshold of 0.25 kg/m^3 from the shallowest observation. This criterion places the mixed layer base atop the zone of strong stratification at the base of the layer where strong velocity shear was frequently observed (Figure 3). Mixed layer depth was only estimated for profiles in which there was a density observation shallower than 12 dbar. Note that stratification above the shallowest ITP-V measurement depth of ~6.5 m or Seaglider measurement is not accounted for in these mixed layer depth estimates.

Richardson number was estimated at a 4-m vertical scale from instantaneous profiles of velocity and density (ITP-V data only, e.g., Figure 4c). Velocity and density profiles were low-pass filtered in the vertical with a 4-m scale, and differences were then taken over a 4-m vertical distance: $Ri_4 = \frac{g\Delta\rho}{\rho_0 \Delta z} / \left(\frac{\Delta u^2}{\Delta z} + \frac{\Delta v^2}{\Delta z} \right)$. The 4-m vertical
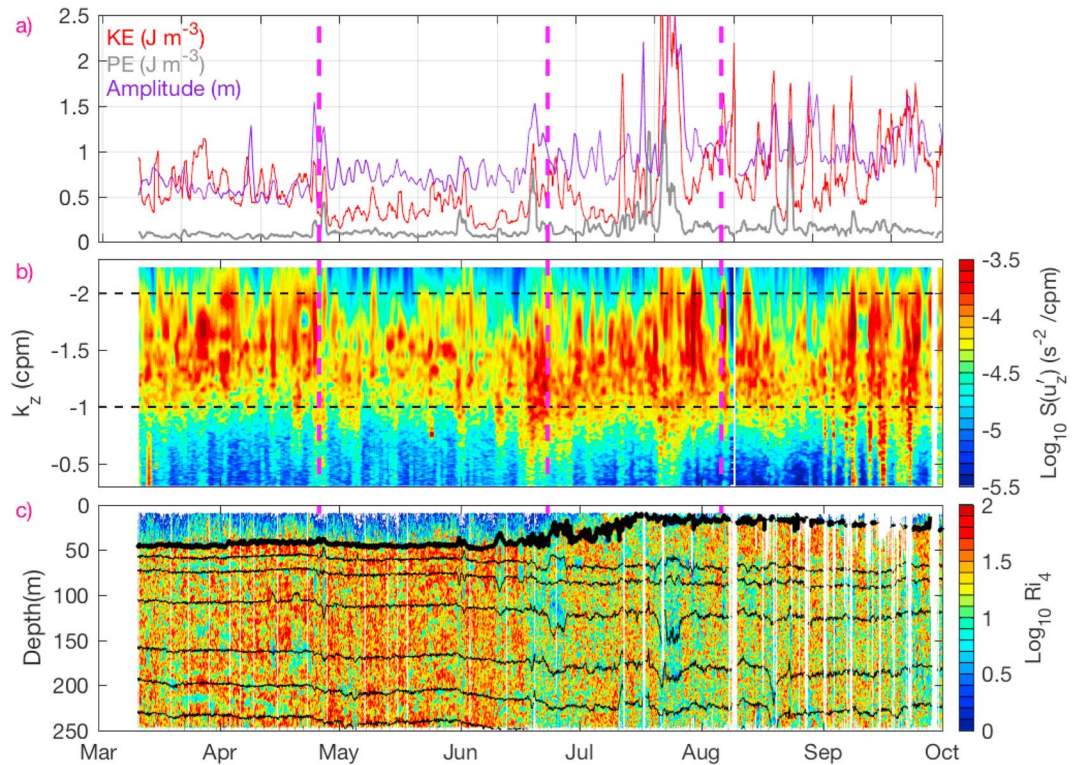
Figure 4. Time series at C2 of (a) near-inertial wave amplitude and daily averaged high-pass filtered kinetic and potential energy vertically averaged over 70- to 240-m depth, (b) daily averaged WKB-scaled vertical wavenumber spectra of high-pass filtered velocity shear over 70- to 240-m depth with the 10- and 100-m WKB-stretched vertical scales indicated (dashed black), and (c) the 4-m Richardson number with mixed layer depth and density surfaces as in Figure 3. Dashed magenta lines as in Figure 2. WKB = Wentzel-Kramers-Brillouin; KE = kinetic energy; PE = potential energy.

scale corresponds to the scale at which the slope of the vertical wavenumber spectra of velocity shear begin to flatten (not shown).

3.2. High-Pass Filtered Profiles

High-pass filtered in time ice and ocean velocity was considered (e.g., Figure 3). A 24-hr filter was used so that near-inertial motions were effectively captured, and lower temporal and/or spatial variations were excluded, including the majority of elevated velocities associated with eddies (e.g., Figure 3b). Such filtering was judged preferable to fitting directly to specified frequencies as the fitted estimate was found to be sensitive to the specific frequencies chosen (Appendix A). High-pass filtered ocean velocities are denoted as u' and referred to as near-inertial motions as this is the dominant high-frequency velocity signal (Figure 5). Although the M2 tidal period is similar at these latitudes (12.37–12.53 hr at C2–C4 for the inertial period versus 12.42 hr for the M2 tidal period), the preference for clockwise in time motions at these frequencies (Figure 5) supports the interpretation of high-frequency velocity features as primarily near inertial (as with previous studies, e.g., Martini et al., 2014).

Internal wave potential and kinetic energy were estimated from the high-pass filtered velocity and isopycnal displacement data. Kinetic energy is estimated as $KE = \frac{1}{2}\rho_0\left(u'^2 + v'^2\right)$, and potential energy as $PE = \frac{1}{2}\rho_0 N^2 \zeta'^2$, where ρ_0 is a reference density taken to be the average density over 70- to 240-m depth (1026.4 kg/m³), N is the instantaneous buoyancy
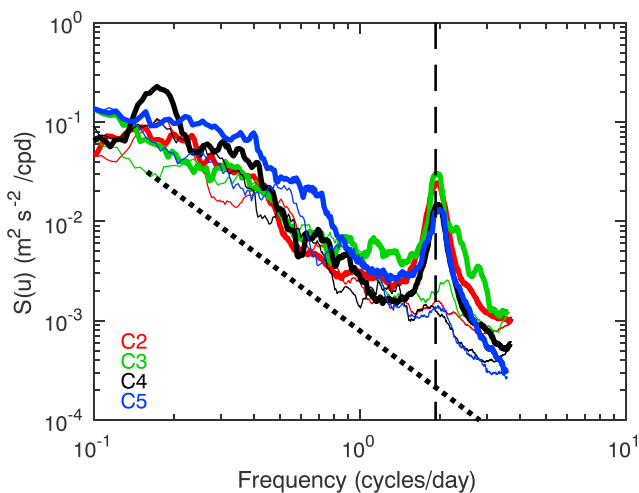
Figure 5. Frequency spectra of velocity, $S(u)$, over 70- to 240-m depth and averaged over the entire deployment. Clockwise (thick) and counterclockwise with time (thin) components are shown. The dotted line has a slope of −2. Three vertical dashed lines (black) are plotted and overlay each other: the near-inertial frequency at 73.3 and 75.5°N and the M2 tidal frequency.
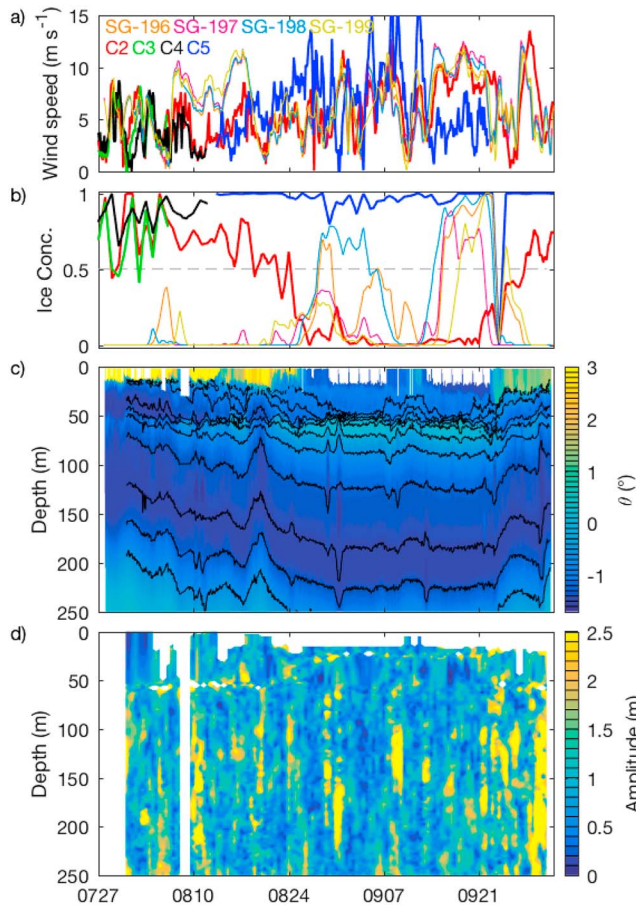
Figure 6. Time series over 27 July to 2 October of (a) Seaglider and ITP-V wind speed, (b) Seaglider and ITP-V ice concentration, (c) Seaglider-198 potential temperature in the upper 250 m with density surfaces every 0.5 kg/m³, and (d) Seaglider-198 near-inertial wave displacement amplitude.

frequency, ζ is the vertical isopycnal displacement, and primed quantities denote the high-pass filtered component (Gill, 1982). Kinetic and potential energy were estimated for each ITP-V profile and then the daily averaged kinetic and potential energy were considered (e.g., Figure 4a).

Vertical wavenumber spectra were constructed over 70- to 240-m depth (e.g., Figure 4b) where there were no observed seasonal changes in stratification. Wentzel-Kramers-Brillouin (WKB; Leaman & Sanford, 1975)-scaled velocity $(u'(N_0/N(z,t))^{1/2})$ was constructed from high-pass filtered velocity profiles using both a constant $N_0 = 1.1 \times 10^{-2}$ rad/s¹ (the average stratification over 70- to 240-m depth and all profiles and clusters) and a time-varying $N(z,t)$ equivalent to observed stratification smoothed with a 7-day timescale. Stretched depth is also utilized to estimate velocity shear $(\int N_0^{-1} N(z,t)dz)$, and so spectra are a function of stretched vertical wavenumber. WKB scaling primarily accounts for variations of stratification with depth and summer mixed layer shoaling (seasonal changes above 70-m depth). Shear spectra, $S(u'_z)$, were computed by Fourier transforming each WKB-scaled shear profile. Clockwise and counterclockwise turning with depth components were separated using a rotary spectral decomposition (Gonella, 1972). The 90% confidence interval was constructed assuming that the number of degrees of freedom at each stretched vertical wavenumber was equivalent to the record length (170 m) divided by the stretched vertical wavenumber and that profiles more than 12 hr apart were independent.

### 3.3. Internal Wave Vertical Displacement Amplitude

For comparison with previous studies of internal-wave amplitude from ITPs (Dosser & Rainville, 2016; Dosser et al., 2014), near-inertial internal wave vertical displacement amplitude is estimated following Dosser et al. (2014) for ITP-V and Seaglider density profiles. Briefly, the vertical displacement time series, η', is defined as the vertical displacement of a given isopycnal from its daily average depth. At each depth, η' is fit to a sinusoid with frequency ω and phase ϕ to determine the internal wave amplitude $A(z,t)$:

$$\eta'(t) = A(z,t)\cos(-\omega t + \phi). \tag{1}$$

The internal wave amplitude represents half the peak-to-trough displacement of isopycnals by internal waves with frequency ω. Data are fit in running segments that are 4 days in duration and 5 vertical bins (5 m in the vertical). One estimate of wave amplitude is made for each day of data. The fitted frequency is taken to be $\omega = 1.05f$, where f is the inertial frequency at the measurement latitude. The fit is only trusted if it explains at least 25% of the variance in the vertical displacement (see Dosser et al., 2014). For the ITP-V and Seaglider records as a whole, the average variance explained was 71% and 74%, respectively. Internal wave amplitude was considered over 70- to 200-m depth (e.g., Figure 6d).

4. Results

Beneath the mixed layer, near-inertial motions were a dominant feature of the velocity field throughout the record (Figure 3). Frequency spectra exhibited a peak about the inertial frequency for the clockwise rotating in time component only (Figure 5). Throughout the MIZ measurement period, the ratio of kinetic to potential energy estimates was consistent with near-inertial motions: utilizing $\frac{KE}{PE} = \frac{\omega^2 + f^2}{\omega^2 - f^2}$ (Fofonoff, 1969; Lien & Müller, 1992), 50% of the kinetic to potential energy ratios over 70- to 240-m depth at C2–C4 corresponded to values between $\omega = 1.00f$ and $\omega = 1.09f$. Throughout the record at C2–C5, velocity shear was elevated at vertical
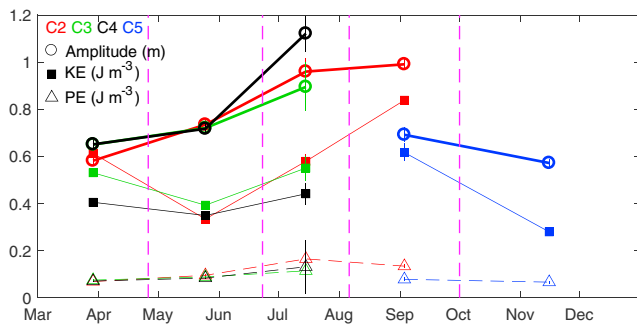
Figure 7. Median (symbols) ± standard error (vertical lines) of near-inertial wave amplitude (thick), daily averaged high-pass filtered kinetic energy (thin), and potential energy (dashed) at C2–C5. The vertical average over 70- to 240-m depth is taken prior to calculating the median value or standard error. Dashed vertical magenta lines as in Figure 2. KE = kinetic energy; PE = potential energy.

scales between 10 and 100 m (Figure 4b), which is typical for the Arctic Ocean (D'Asaro & Morehead, 1991; Pinkel, 2008).

Internal wave properties were modulated at daily to seasonal timescales (e.g., at C2, Figure 4). Day-to-day variability was evident in kinetic energy, potential energy, near-inertial amplitude, and vertical wavenumber spectral level of velocity shear. Brief periods of elevated values were observed throughout the record that relate in part to short-term variations in the wind forcing. However, it is the monthly scale changes to the internal wavefield, which are not directly related to changes in wind forcing that are the focus of the subsequent analysis.

### 4.1. Seasonal Modulations of KE, PE, and Velocity Shear

Five time periods were identified based on conditions of the sea ice field (Figure 2a), the ITP-V sampling, and characteristics of the vertical wavenumber velocity shear spectra (e.g., Figure 4b). These time periods are as follows: March to 26 April, 27 April to 22 June, 23 June to 6 August, 7 August to 30 September, and 1 October to 31 December. The first division between time periods, 26 April, corresponds to the first significant wind event (Figure 2b) and the first decreases in ice concentration during the study (Figure 2a). The next division between time periods, 22 June, corresponds to an abrupt decrease in ice concentration to near ~80% (Figure 2a). The final divisions, 6 August and 30 September, correspond to the dates when near-inertial currents sampling ended at C3 and C2, respectively. October–December is considered for C5.

4.1.1. The 100% Ice Concentration Conditions: March to 26 April

During March to 26 April, KE, PE, and near-inertial amplitude (Figures 7 and 8) were small relative to later time periods but similar to previous Arctic observations (D'Asaro & Morehead, 1991; Dosser & Rainville, 2016; Martini et al., 2014). Probability density functions (PDFs) had values of $KE < 1.5$ J/m^3, $PE < 0.3$ J/m^3, and amplitudes <2 m in this time period (Figure 8).

Shear spectra showed sensitivity to the derived ice-ocean drag coefficient, which was most evident when comparing C4 that had the highest ice-ocean drag coefficient to C2 that had the lowest. C4 (high drag, Table 1) had the largest total energy at all vertical scales smaller than 100 m (Figure 9g) largely due to elevated downward energy propagation (inferring the propagation direction from the dominance of clockwise over counterclockwise rotation with depth). C2 (low drag, Table 1) had the smallest total energy at vertical scales less than 10 m and predominantly upward energy propagation for vertical scales greater than 30 m (Figure 9a). The differences in the spectra between C2 and C4 are consistent with the idea that smoother ice generates fewer or less energetic internal waves, with predominantly upward propagating internal wave energy indicative of a larger percentage of remotely forced internal wave energy propagating into the region than was generated locally.
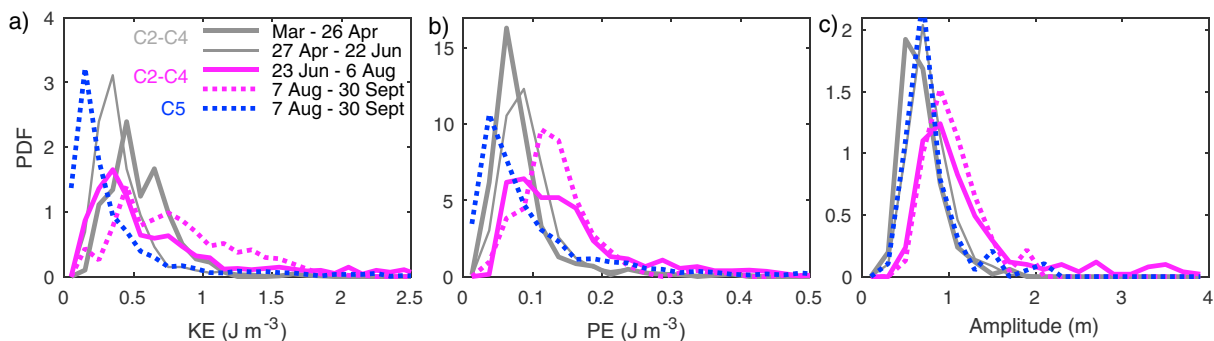
Figure 8. Probability density functions by time period of (a) daily averaged high-pass filtered kinetic energy, (b) daily averaged high-pass filtered potential energy, and (c) near-inertial wave amplitude. Data from C2–C4 are combined (gray and magenta) and vertically averaged over 70- to 240-m depth. PE (high-pass filter) and amplitude (fit to a specific frequency) differ due to methods used. PDF = probability density function; KE = kinetic energy; PE = potential energy.
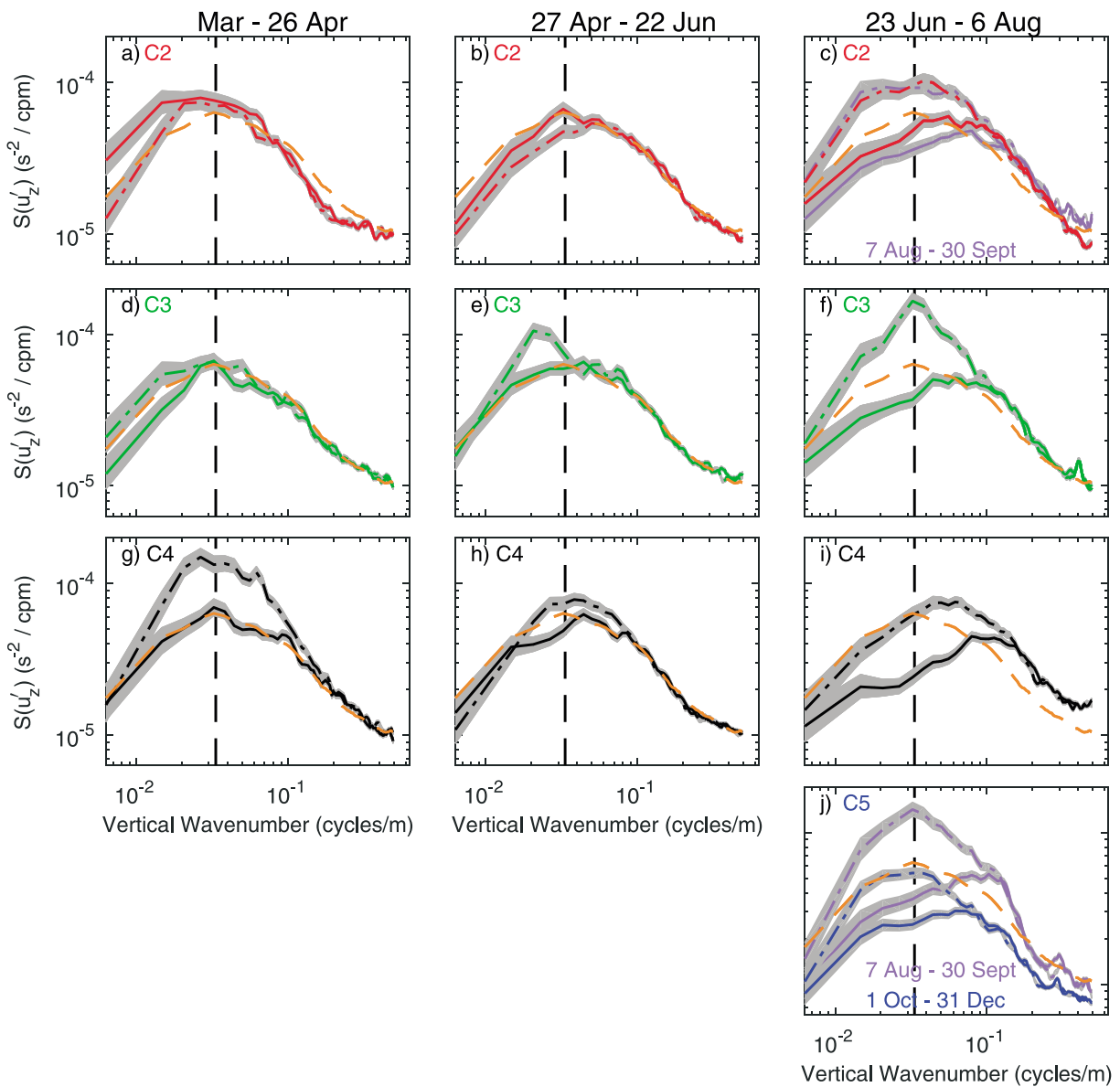
Figure 9. Statistics of WKB-scaled high-pass filtered vertical wavenumber spectra at (a–c) C2, (d–f) C3, (g–i) C4, and (j) C5. WKB-scaled vertical wavenumber spectra over 70- to 240-m depth are averaged over different time periods with upward (counterclockwise with depth; solid) and downward (clockwise with depth; dashed) velocity shear indicated. Gray shading denotes the 90% confidence interval estimated assuming that profiles 12 hr apart in time are independent. Dashed orange line shows the average upward component over C2–C4 and March to 6 August. The dashed vertical line corresponds to a stretched vertical scale of 30 m. Time periods are indicated at the top of each column, with the purple lines in (c) and (j) corresponding to the time period of 7 August to 30 September and blue lines to October to 31 December. WKB = Wentzel-Kramers-Brillouin.

4.1.2. A Fractured Ice Cover: 27 April to 22 June

Seasonal changes in kinetic energy and shear spectra were observed beginning on 26 April when a wind event (Figure 2b) began to break the ice apart (and decrease ice concentration; Figure 2a). Internal wave energy (KE + PE) decreased during 27 April to 22 June (e.g., Figures 4a, 7, 8a, and 8b). Internal wave vertical displacement amplitudes remained small (Figures 7 and 8c). Shear spectra energy levels at scales larger than 30 m decreased for both upward and downward propagating components at C2 (Figures 9a and 9b) and at vertical scales larger than 10 m for downward propagating components at C4 (Figures 9g and 9h). In contrast, energy increased at C3 (Figures 9d and 9e), likely due to the rearrangement of the ice that resulted in ridges and a rougher ice cover in the immediate vicinity of the ITP-V during this time period (Table 1; Figure 6 of Cole et al., 2017). The dominant propagation direction remained upward at C2 and downward at C3 and C4.
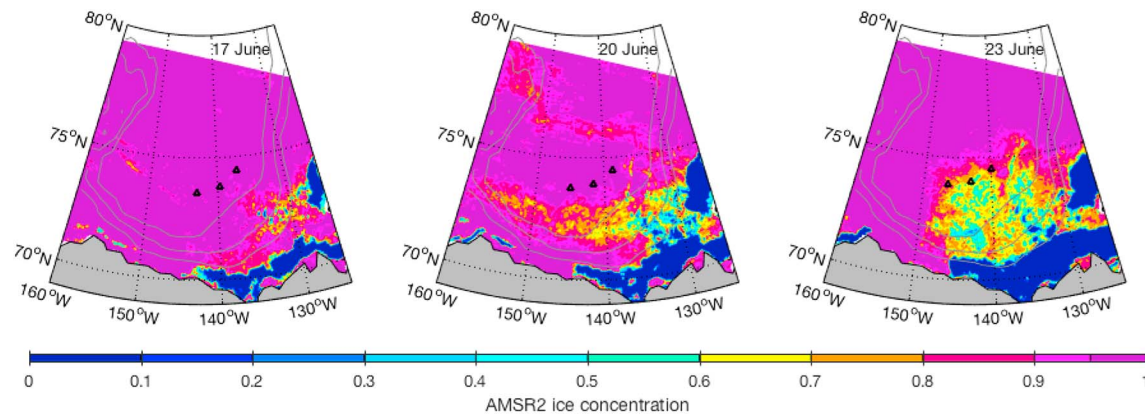
Figure 10. AMSR-2 ice concentration on 17, 20, and 23 June 2014. Locations of C2–C4 are shown as black triangles. AMSR = Advanced Microwave Scanning Radiometer 2.

The *decrease* in energy observed after 26 April at C2 and C4 (Figures 4c and 9) occurred despite a minor *increase* in low-frequency wind and ice velocities after 26 April (Figures 2b and 2c). The primary difference between these two time periods (March to 26 April versus 27 April to 22 June) was the ice cover itself, with the latter time period corresponding to a fractured ice cover (ice concentrations of 96–99%). Compared with a contiguous ice cover, it is physically plausible that a fractured ice cover will dissipate or scatter more internal wave energy during the internal waves' surface reflection from the under-ice topography. This explanation suggests that some internal wave energy is capable of reflecting off of the underside of the ice cover, contrary to the one bounce scenario (Pinkel, 2005), so that both upward and downward energy decrease (without a change required in either the local or remote generation of internal waves). A fractured ice cover appears to have had a greater impact on dissipation during the surface reflection for the smoothest ice (at C2) as there is a greater change in the roughness that an upward propagating internal wave encounters for contiguous, smooth ice that cracks into a fractured surface (versus a contiguous rough ice cover that cracks into a fractured surface). The initial decreases in ice concentration from 100% that began on 26 April increased the dissipation of internal waves during their surface reflection and so decreased the downward as well as subsequent upward propagating internal wave energy.

4.1.3. Decrease Below 80% Ice Concentration: 23 June to 6 August

A significant change was observed after 23 June, when ice concentration decreased below ~80% and the mixed layer shoaled. Shear spectra energy levels (Figures 4b, 9c, 9f, and 9i) and internal wave energy (KE + PE, Figure 7) increased. PDFs of KE, PE, and wave amplitude had larger mean values and a broader distribution over 23 June to 6 August, with an increased fraction of samples achieving high values (Figure 8). These increases in energy coincided with a decrease in ice concentration about all three clusters (C2–C4) from greater than 95% on 20 June to 70–80% on 23 June (Figure 10). Ice concentration then remained between ~60% and 95% during 23 June to 6 August (Figure 2a).

Shear spectra energy levels exhibited several consistent changes across C2–C4 during 23 June to 6 August. At C2–C4, shear spectra energy levels increased for downward propagating internal waves at vertical scales smaller than 30 m and for upward propagating internal waves at vertical scales smaller than 10 m (Figures 9b and 9c, 9e and 9f, and 9h and 9i). At C2, the ratio of upward to downward shear spectra energy levels changed to predominantly downward energy propagation and the ratios at C3 and C4 remained predominantly downward. The increase in downward propagating internal wave energy at a range of vertical length scales, and all ice roughness conditions (C2–C4), suggests that the decreased ice concentration led to increased local generation.

4.1.4. Contrasting Ice Concentrations: 7 August to 30 September

Observations at C2 and C5 over 6 August to 30 September show how ice concentration, which was 90–100% at C5 and approaching open water at C2, influenced internal wave properties. PDFs show values of KE, PE, and wave amplitude at C5 that were smaller than at C2 and similar to those found at C2–C4 over March to 26 April when ice concentration was 97–100% (Figure 8). Shear spectra were not as distinctly different with less energy at C5 than at C2 for the upward component at most vertical scales and comparable energy for the
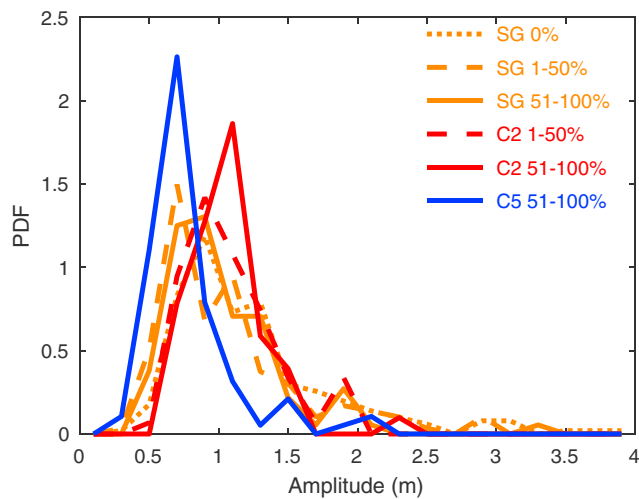
Figure 11. PDFs of near-inertial wave amplitude averaged over 70- to 200-m depth during 27 July to 2 October. All Seaglider data (orange), C2 (red), and C5 (blue), for open water (dotted), ice concentrations less than 50% (excluding open water; dashed), and ice concentrations greater than 50% (solid). For C2, no data are considered to be observed in open water. PDF = probability density function.

downward component at most vertical scales (Figures 9c and 9j). It may be that the large ice-ocean drag coefficient estimated at C5 at this time largely compensated for decreased energy input inferred from the larger ice concentrations (as suggested by its similarity to C4 winter conditions, Figure 9g). C5 also had the largest tendency toward downward propagation compared with C2–C4, potentially due to the combination of rough ice and shallow summer mixed layers. Internal wave properties appear to be more sensitive to changes in ice concentration than (1) mixed layer depth, which had median values of 25 m at C5 during 7 August to 30 September and 40 m at C2–C4 during March to 26 April, (2) the higher latitude at C5 that would imply decreased internal wave activity (Dosser & Rainville, 2016), or to a lesser extent (3) the greater ice roughness at C5 (Table 1) that would suggest increased local generation.

Shear spectra at C2 also illustrate that internal wave energy is *not* sensitive to some changes in ice concentration. At C2, shear spectra over 7 August to 30 September were comparable to those over 23 June to 6 August (Figure 9c), showing that further decreases in ice concentration below 70–80% (to less than 30% during late August and early September) did not lead to a further increase in internal wave activity.

4.1.5. Return to High Ice Concentration: 1 October to 31 December

Shear spectra at C5 over October to December were less energetic than over 7 August to 30 September, potentially due to larger ice concentrations or deeper mixed layers but retained the tendency of excess downward propagation. The large tendency toward predominantly downward propagation throughout the C5 record is consistent with rougher ice locally generating more internal wave energy.

4.2. Open Water and Internal Wave Displacement Amplitude

To investigate how the internal wavefield differs between open water and the MIZ, we compare near-inertial wave vertical displacement amplitude from ITP-Vs within the MIZ and Seaglider observations that spanned open water as well as the MIZ. This comparison is limited to the times where Seagliders were in operation, 27 July to 2 October, and primarily to data from C2 and C5 (Figure 1b). Open water and MIZ conditions differed, with mixed layer temperature in areas of open water that was 2–3 °C warmer than beneath the ice cover (Figure 6c) and mixed layer depths that were slightly shallower at ~10–15 m in open water versus ~15–20 m beneath sea ice (e.g., Figure 6c). Further details of upper ocean stratification across the MIZ will be discussed in a separate paper. There were no apparent differences between open water and ice-covered regions within the Seaglider data set or between the Seaglider and ITP-V data sets for wind speed (Figure 6a) or stratification (not shown). The near-inertial wave vertical displacement amplitudes over 27 July to 2 October for both Seagliders and at C2–C5 were highly variable (e.g., Figure 6d), with episodically elevated values throughout the record, often in response to stronger wind forcing conditions.

As the Seagliders and ITP-Vs observed different ice concentrations at any given time (Figure 6b), PDFs of wave amplitude were constructed based on the fraction of open water (Figure 11). In the Seaglider data, a clear change in amplitude is observed with open water conditions having the largest wave amplitudes (mean value of 1.3 m; Table 2). Seaglider and C2 amplitudes statistics were similar to each other and smaller than open water conditions for ice concentrations of 1–50% (mean value of 1.1 m) and 51–100% ice concentration (mean value of 1.0 m; Figure 11 and Table 2). C5, with ice concentrations above 90%, had a mean amplitude of 0.8 m, similar to the mean value of 0.7 m observed at C2–C4 during March to 26 April (Figure 8c). In comparison to the full ice cover conditions at C2–C4 during March to 26 April, the open water mean Seaglider internal wave amplitude was 80% larger, and the 1–50% ice concentration ITP-V and Seaglider values were 60% larger.

Table 2
Mean ± 95% Confidence Internal of the Internal Wave Amplitude in Meters for Open Water, 1–50% Ice Concentration, and 51–100% Ice Concentration Conditions

Ice concentration	Seagliders	C2[a]	C5[a]
Open water	1.3 ± 0.1	—	—
1–50%	1.1 ± 0.1	1.1 ± 0.1	—
51–100%	1.0 ± 0.1	1.0 ± 0.1	0.8 ± 0.1

[a]Only the time period of 27 July to 2 October is considered.
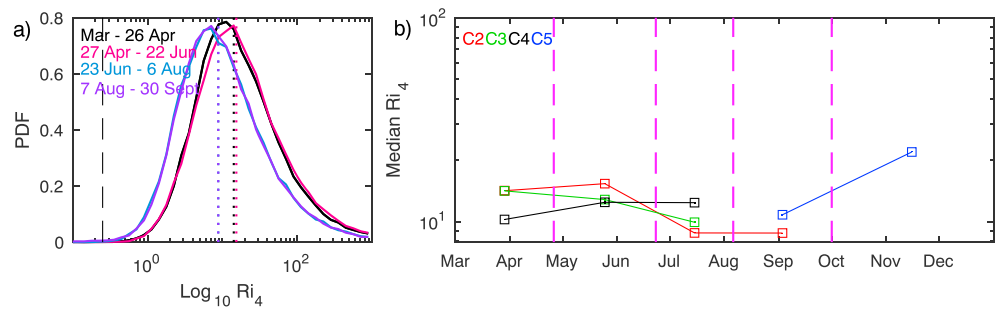
Figure 12. Statistics of the 4-m Richardson number. (a) PDFs by time period at C2. The dashed black line shows a value of $Ri = 1/4$. Dotted lines show the median value. (b) Median value by cluster and time period. Dashed magenta lines as in Figure 2. PDF = probability density function.

4.3. Richardson Number

The 4-m Richardson number is first considered at C2. PDFs over 70- to 240-m depth by time period show that the 4-m Richardson number was larger than 1/4 (the necessary but not sufficient condition for instability) for all but a handful of points near the tail of the distribution (Figure 12a), indicating that vertical mixing was weak regardless of the ice cover. The variations between time periods are well characterized by the median Richardson number within each time period (Figure 12a).

Richardson numbers at C3–C5 were similar to those at C2 (Figure 12b). Seasonal modulations of Ri_4 were minor, with the largest values observed during periods with low shear spectra energy levels and internal wave activity at C2 during 27 April to 22 June, C4 during 23 June to 6 August, and C5 during October to December (Figure 12b). Overall, differences in ice roughness between clusters or ice concentration between time periods had only small effects on the Richardson number. During 23 June to 30 September 0.2% of Ri_4 values were smaller than ¼ (not shown), indicating that vertical mixing at these 4-m scales was occasionally possible.

5. Discussion

This analysis has shown the advantage of investigating the internal wavefield while following the ice cover. It was by following different patches of ice, each with distinguishable ice roughness characteristics through the same forcing conditions, that the influence of ice roughness on the internal wavefield was revealed. The Lagrangian tracking of multiple points makes this a more complete data set compared with past observations. It is worth noting that deployment in ice patches having contrasting ice roughness properties was not a factor in the choice of deployment location but occurred fortuitously. Observations from the contrasting ice concentrations provided by C2 and C5 were also necessary to at least partially separate the influence of ice concentration from seasonally varying mixed layer depth and stratification. While the ITP-Vs did not completely melt out into open water, the joint analysis of ITP-V and Seaglider data fully spans the parameter space from open water to 100% ice cover as well as encompassing a variety of ice roughness conditions.

While internal wave properties clearly depend on ice concentration with distinct differences in energy between full ice cover and the lowest ice concentrations, there was little dependence for the wide range of ice concentrations indicative of the MIZ (approximately 15–80% ice concentration). Overall, there was an 80% increase in internal wave amplitude between full ice cover (amplitudes of 0.7 m at C2–C4 in March to 26 April) and open water (1.3 m for Seagliders in August–September), greater than the seasonal cycle documented in Dosser and Rainville (2016) as that measure includes a variety of ice concentrations in the summer season. The open water conditions observed by the Seagliders had amplitudes 20% larger than the low ice concentration conditions observed at C2, consistent with past studies showing less dramatic contrasts between low ice concentrations and open water conditions (Randelhoff et al., 2017). The specific mechanism that results in increased energy between low ice concentrations and open water is unclear; decreased dissipation at the surface (due to absence of rough ice or a lack of any ice) or increased local generation is plausible.

Ice concentration was considered at a 30-km scale (15-km radius) to show its seasonal evolution; however, the relevant scale for the internal wavefield may be different and potentially seasonally evolving. From the dispersion relation, internal waves with vertical scales of 10–100 m and frequencies of 1–1.2f have horizontal scales ranging from ~1 to 100 km. It is the cracks in the ice cover (at high ice concentration) or the collection of individual floes (at lower ice concentrations) at this 1- to 100-km scale that is relevant to the dissipation during reflection from the under-ice surface. Internal wave generation may also be influenced by the horizontal size of individual ice floes, which evolve spatially and seasonally (Hwang et al., 2017).

There is a potential alternative explanation for the transition in internal wave characteristics in late June (ice concentrations below 70–80%), as it occurred very close to the onset of bottom melt (~15 June; see Figure 4 of Cole et al., 2017), melt pond drainage (27 June; see Gallaher et al., 2016), and mixed layer shoaling (shallower than 20 m by 8 July; see Figure 9 of Cole et al., 2017). A shallow mixed layer, or an ephemeral 1- to 2-m-thick fresh layer of melt water, could increase internal wave generation by bringing stratified regions into contact with even modest draft ice ridges (McPhee & Kantha, 1989). At the same time, a shallower mixed layer would also result in larger internal wave velocities at the surface boundary condition with the ice and so increased dissipation (Guthrie et al., 2013; Morison et al., 1985). It is the observations at C5, which had comparable upper ocean stratification but differing ice concentrations, that suggest that ice concentration is the controlling factor and not seasonal changes in surface layer stratification. We find no clear evidence in the MIZ observations that mixed layer shoaling influenced the internal wavefield.

Ice roughness appeared important to the internal wavefield only for ice concentrations greater than 70–80%. Observations in 100% ice concentration were consistent with the theories that (1) smoother ice does not locally generate as much internal wave energy and (2) some or all of the internal wave energy dissipates during the surface reflection from the ice cover. The first cracks in the ice cover, when ice concentration decreased from 100% to 95–99%, were associated with decreased internal wave energy for both upward and downward propagating energy, suggesting that (1) dissipation and/or scattering during the surface reflection was larger for a fractured ice cover and (2) some fraction of the internal wave energy propagates through multiple surface and bottom reflections in contrast to the one bounce scenario of internal wave propagation (Pinkel, 2005). The previous two points imply that horizontal propagation distances will be shorter beneath ice concentrations of ~80–99% compared with 100% ice concentration. The decreased energy beneath a fractured ice cover was most pronounced for the smoothest ice cover (C2) but still evident for rougher ice (C4), suggesting that ice roughness influences the seasonality of the internal wavefield. Cluster 3 did not show this same decrease in energy because the ice roughness increased simultaneously with the first cracks in the ice cover (Table 1; see also Cole et al., 2017). There was no evidence that ice roughness influenced the internal wavefield once there was sufficient open water to increase local internal wave generation.

The observations of predominantly upward energy propagation at C2 lasting for more than a month are distinct from the majority of past studies that found predominantly downward propagation or an approximately equal proportion of upward and downward fluxes (Cole et al., 2014; D'Asaro & Morehead, 1991; Fer, 2014; Halle & Pinkel, 2003; Pinkel, 2005; Martini et al., 2014). Upward energy propagation had only been observed previously near topographic features (e.g., D'Asaro & Morison, 1992; Fer et al., 2010) and for a period of a few days during which internal waves interacted with strong (>0.05 m/s) subinertial shear (Merrifield & Pinkel, 1996). C2 was not located near any significant topographic features during March to 22 June, and the subinertial currents were smaller than 0.05 m/s (with the exception of eddies). It is more likely that the smooth ice cover reduced the local generation of internal waves leaving the upward propagation from more remotely generated waves to dominate the velocity shear signal.

The conclusions regarding the role of ice roughness are obtained largely through comparative arguments between two systems (C2 and C4 primarily), and the MIZ dataset certainly does not span the full parameter space. The findings presented regarding ice roughness are not simply inferences or suggestions as we find no other physically plausible way to interpret the observations than by invoking arguments regarding the (order-one) role of ice roughness. A suite of order 10 ITP-V systems, all with different ice roughness conditions, would allow for a comprehensive view from smooth first-year ice to rough multiyear ice of the influence of ice roughness on internal wave generation, propagation, and dissipation. Ice roughness should also be more routinely considered and reported for any study of internal waves beneath sea ice.

The results of this study have implications for seasonal to decadal-scale changes in the internal wavefield. On decadal timescales, Guthrie et al. (2013) did not detect any changes in internal wave energy even though the ice cover had changed dramatically (including an increase in periods of open water conditions). This stability was attributed to increasing stratification and a shallower mixed layer on a decadal scale that decreased internal wave energy, offsetting the increased internal wave energy from increased areas and times of open water. The interplay between ice concentration and ice roughness observed during these 2014 observations suggests that decadal scale changes in ice roughness will also impact internal wave energy levels, with some of the increase in internal wave energy potentially offset by a smoother (first-year) ice cover that generates fewer and/or less energetic internal waves. The role of ice roughness on a decadal scale is complex, as smoother ice will generate fewer internal waves and will also allow those generated waves to propagate longer distances under full ice cover, potentially leading to increased dissipation at the basin boundaries. Dissipation at the basin boundaries may also change seasonally due to seasonal changes in ice concentration with a fractured ice cover limiting propagation distances. Like the ice cover, the internal wavefield is becoming increasingly seasonal and so decadal scale observations of the internal wavefield must consider such seasonal changes. These observations show that the annually averaged internal wave energy will depend on the areas and times of open water, as well as the areas and times with ice concentrations less than 80% (e.g., the expanding MIZ), ice roughness during periods with ice concentrations of 80–100%, and possibly mixed layer depth.

The importance of the seasonal and/or decadal changes in the internal wavefield to ocean stratification and the ice cover depends on the extent to which such changes influence vertical mixing (of density and heat). From our observations, Richardson number provides only some constraints on the possible variations in vertical mixing. The 4-m Richardson number was almost always larger than 1/4 during the MIZ field program, consistent with the paradigm of weak turbulent diapycnal diffusivities in the Arctic (e.g., Fer, 2009; Guthrie et al., 2013; Lincoln et al., 2016; Randelhoff et al., 2017). Lower values were observed for rougher ice and lower ice concentrations, suggesting that vertical mixing may be sensitive to changes in the ice cover. The broad picture of weak vertical mixing and sensitivity to the ice cover is independent of the specific vertical scale chosen at which to estimate the Richardson number (e.g., 1 m versus 4 m versus 10 m), although the Richardson numbers themselves do vary. The Richardson number would be ideally estimated at the Ozmidov scale ($(\epsilon N^{-3})^{1/2}$), which is smaller than 1 m for $N = 1.1 \times 10^{-2}$ rad/s, a dissipation rate of 10^{-8} to 10^{-10} W/kg (Fer, 2014; Lincoln et al., 2016). Vertical mixing may not be best parameterized or investigated from statistics at a 10 m or even a 1-m vertical scale. It is also clear from these observations that internal wave amplitudes were largest, and Richardson numbers were smallest in closed eddies (Figures 3b, 3c, and 5d), consistent with past studies of eddies' effects on internal waves (e.g., Kunze, 1985; Kunze et al., 1995). The conclusions regarding large Richardson numbers and weak vertical mixing are only relevant to the specific depth range of 70–240 m, which encompasses the lower portions of Pacific Summer Water and some of the lightest Atlantic Water. Changes in the internal wavefield may have the most significant role to play in the region closest to the mixed layer base in the upper 70 m. Direct turbulence observations are needed to better understand the extent to which ice roughness, ice concentration, and eddy activity influence vertical mixing.

6. Summary and Conclusions

Canada Basin observations of ocean velocity, stratification, and isopycnal displacement throughout an Arctic melt season were used to investigate the nature of the internal wavefield in the stratified waters below the mixed layer base. These observations confirm the paradigm of persistently weak vertical mixing (Fer, 2009; Guthrie et al., 2013; Lincoln et al., 2016; Rainville & Windsor, 2008) in the Arctic Ocean:

1. Observed Richardson number at a 4-m scale under all ice concentrations and ice roughness characterizations rarely fell below ¼ but was sensitive to ice concentration and roughness. Richardson numbers were smallest in the vicinity of closed eddies.

Also consistent with past studies, we find that internal wave energy was largest in open water (in agreement with, e.g., Dosser and Rainville 2016) and that energy dissipates during the surface reflection from the under-ice topography (as in Pinkel, 2005).
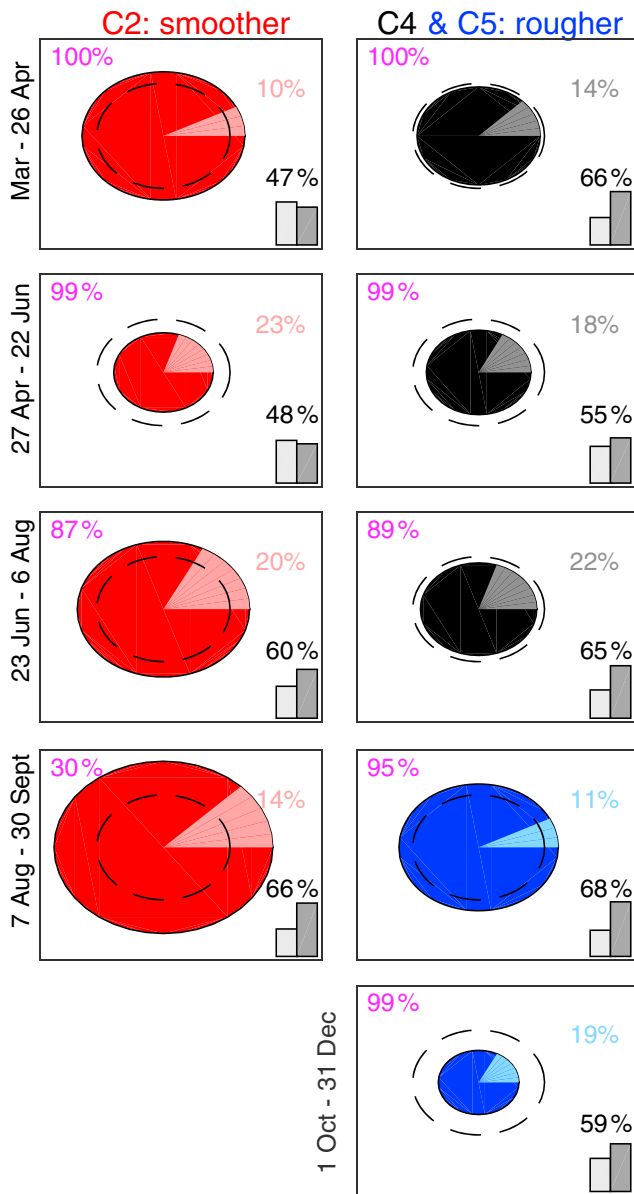
Figure 13. Summary for C2 (red), C4 (black), and C5 (blue) of the kinetic (red, black, and dark blue) and potential (pink, gray, and light blue) energy by time period. The dashed circle corresponds to a total energy of 0.5 J/m³. The mean AMSR-2 ice concentration in each time period is in magenta. Gray vertical bars show the percentage of velocity shear at vertical scales larger than 10 m that is downward (dark gray, percentages) and upward (light gray). AMSR = Advanced Microwave Scanning Radiometer 2.

This study refines the paradigm that ice concentration and mixed layer depth are the key factors determining internal wave properties as follows:

1. Internal wave energy experienced abrupt transitions when the ice concentration first decreased from 100%, reached ~70–80%, and in open water conditions. The distinct transitions indicate that there is both a dependence and an independence on ice concentration, with the specific ice concentration in the ~15–80% range less relevant than other factors.
2. Internal wave energy was smallest for ice concentrations near but not at 100%, likely due to increased dissipation during the surface reflection when the ice cover is fractured.
3. Some energy is able to reflect from the under-ice topography during the surface reflection, especially at the largest vertical scales.
4. Ice roughness was most influential for ice concentrations greater than ~80%. The smoothest ice had weaker energy levels consistent with weaker local generation of internal waves and exhibited the largest seasonal cycle in energy levels. There was no evidence that ice roughness influenced the internal wavefield once ice concentrations decreased below ~80%.

The internal wave conditions are summarized in Figure 13, which compares the smooth conditions of C2 to the rougher conditions of C4 and C5 for the various time periods. These conclusions show the interplay between ice concentration and ice roughness that complicates future predictions of internal wave activity and vertical mixing. It is the transitions to ~70–80% ice concentration and to open water that appear most influential and that differences in ice roughness can be as significant as such transitions in ice concentration.

The MIZ experiment observations sampled within the parameter space of ice roughness, ice concentration, and shallow stratification, but this parameter space has not been fully explored. Observations that span the full range of ice roughness from first-year ice to multiyear ice are needed in particular to quantify the extent to which smooth ice reduces local generation as well as local dissipation. The transition of the ice cover from ~80% ice concentration to near-open water conditions occurred rapidly over a few weeks, and while there was no indication of overall changes in energy level, changes to internal wave generation that were balanced by changes to dissipation may have occurred. The consistently large Richardson numbers suggest that vertical mixing in the Arctic interior takes place primarily at vertical scales smaller than 4 m. Past analyses based on the 10-m vertical scale should be carefully considered, and future studies should additionally investigate smaller vertical scales. Direct observations of turbulent mixing beneath contrasting ice concentration and ice roughness conditions are needed to assess changes to vertical mixing and the influence of internal wave properties on ice melt/growth and the overall stratification of the Arctic Ocean.

Appendix A: Estimation of Near-Inertial Currents

Two methods for estimating near-inertial currents are considered. One measure of high-frequency currents is a 24-hr high-pass filtered velocity record. This estimate ignores the minor irregularities in the timing of measurements due to the 15–20 mins required to complete a profile; for example, at 80-m depth, data acquired during the upgoing and downgoing profiles are spaced apart by 2.9 and 3.1 hr for 250-m profiles and by 2.4 and 3.6 hr when a 750-m profile is taken. Differences between a 24-hr period and twice the inertial period
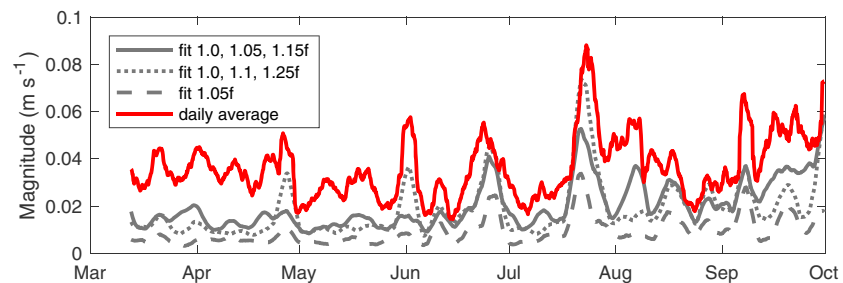
Figure A1. Magnitude of high-frequency velocity averaged with a 4-day timescale at 80-m depth for C2. Different methods of defining high-frequency currents are compared: Gray curves correspond to harmonic fits with different frequencies over 4-day segments of data, and the red curve corresponds to a 24-hr high-pass filter.

(12.37 to 12.53 hr at these latitudes) are also ignored. A second estimate is constructed by fitting velocity components to specified frequencies, which specifically accounts for the irregular timing between profiles. Three frequency combinations are considered: (1) f, $1.05f$, and $1.15f$; (2) f, $1.1f$, and $1.25f$; and (3) $1.05f$.

The high-pass filtered product was deemed preferable for this analysis. Fitting to the frequencies of f, $1.05f$, and $1.15f$ agreed best with the filtered estimate, with magnitudes that were occasionally significantly smaller (Figure A1). As the fitted estimate was sensitive to the specific frequencies chosen, the high-pass filtered velocity estimate is utilized in this analysis. The features of interest are insensitive to the method chosen to define near-inertial signals: there was good agreement in pattern between high-pass filtered potential energy and near-inertial internal wave amplitude (e.g., Figure 4a), which is estimated by fitting to a single frequency.

References

Cole, S. T., Thwaites, F. T., Krishfield, R. A., & Toole, J. M. (2015). Processing of velocity observations from Ice-Tethered Profilers. In *MTS/IEEE Oceans' 2015 conference*. Washington, DC, 1-10.

Cole, S. T., Timmermans, M.-L., Toole, J. M., Krishfield, R. A., & Thwaites, F. T. (2014). Ekman veering, internal waves, and turbulence observed under Arctic Sea ice. *Journal of Physical Oceanography*, 44(5), 1306–1328. https://doi.org/10.1175/JPO-D-12-0191.1

Cole, S. T., Toole, J. M., Lele, R., Timmermans, M.-L., Gallaher, S. G., Stanton, T. P., et al. (2017). Ice and ocean velocity in the Arctic marginal ice zone: Ice roughness and momentum transfer. *Elementa: Science of the Anthropocene*, 5, 55. https://doi.org/10.1525/elementa.241

D'Asaro, E. A., & Morehead, M. D. (1991). Internal waves and velocity fine structure in the Arctic Ocean. *Journal of Geophysical Research*, 96(C7), 12,725–12,738. https://doi.org/10.1029/91JC01071

D'Asaro, E. A., & Morison, J. H. (1992). Internal waves and mixing in the Arctic Ocean. *Deep Sea Research*, 39, 5459–5484.

Dosser, H. V., & Rainville, L. (2016). Dynamics of the changing near-inertial internal wave field in the Arctic Ocean. *Journal of Physical Oceanography*, 46(2), 395–415. https://doi.org/10.1175/JPO-D-15-0056.1

Dosser, H. V., Rainville, L., & Toole, J. M. (2014). Near-inertial internal wave field in the Canada Basin from Ice-Tethered Profilers. *Journal of Physical Oceanography*, 44(2), 413–426. https://doi.org/10.1175/JPO-D-13-0117.1

Eriksen, C., Osse, T., Light, R., Wen, T., Lehman, T., Sabin, P., et al. (2001). Seaglider: A long-range autonomous underwater vehicle for oceanographic research. *IEEE Journal of Oceanic Engineering*, 26(4), 424–436. https://doi.org/10.1109/48.972073

Fer, I. (2009). Weak vertical diffusion allows maintenance of cold halocline in the Central Arctic. *Atmospheric and Oceanic Science Letters*, 2(3), 148–152. https://doi.org/10.1080/16742834.2009.11446789

Fer, I. (2014). Near-inertial mixing in the central Arctic Ocean. *Journal of Physical Oceanography*, 44(8), 2031–2049. https://doi.org/10.1175/JPO-D-13-0133.1

Fer, I., Skogseth, R., & Geyer, F. (2010). Internal waves and mixing in the marginal ice zone near the Yermak Plateau. *Journal of Physical Oceanography*, 40(7), 1613–1630. https://doi.org/10.1175/2010JPO4371.1

Fofonoff, N. P. (1969). Spectral characteristics of internal waves in the ocean. *Deep Sea Research*, 16(Suppl), 58–71.

Gallaher, S. G., Stanton, T. P., Shaw, W. J., Cole, S. T., Toole, J. M., Wilkinson, J. P., et al. (2016). Evolution of a Canada Basin ice-ocean boundary layer and mixed layer across a developing thermodynamically forced marginal ice zone. *Journal of Geophysical Research*, 121, 6223–6250. https://doi.org/10.1002/2016JC011778

Gill, A. E. (1982). *Atmosphere-ocean dynamics* (p. 662). London: Academic Press.

Gonella, J. (1972). A rotary-component method for analyzing meteorological and oceanographic vector time series. *Deep Sea Research*, 19, 833–846.

Guthrie, J. D., Morison, J. H., & Fer, I. (2013). Revisiting internal waves and mixing in the Arctic Ocean. *Journal of Geophysical Oceanography*, 118, 3966–3977.

Halle, C., & Pinkel, R. (2003). Internal wave variability in the Beaufort Sea during the winter of 1993/1994. *Journal of Geophysical Research*, 108(C7), 3210. https://doi.org/10.1029/2000JC000703

Hwang, B., Wilkinson, J., Maksym, T., Graber, H. C., Schweiger, A., Horvat, C., et al. (2017). Winter-to-summer transition of Arctic sea ice breakup and floe size distribution in the Beaufort Sea. *Elementa: Science of the Anthropocene*, 5(40), 1–25.

Kunze, E. (1985). Near-inertial wave propagation in geostrophic shear. *Journal of Physical Oceanography*, 15(5), 544–565. https://doi.org/10.1175/1520-0485(1985)015<0544:NIWPIG>2.0.CO;2

Kunze, E., Schmitt, R. W., & Toole, J. M. (1995). The energy balance in a warm-core ring's near-inertial critical layer. *Journal of Physical Oceanography*, 25(5), 942–957. https://doi.org/10.1175/1520-0485(1995)025<0942:TEBIAW>2.0.CO;2

Leaman, K. D., & Sanford, T. B. (1975). Vertical energy propagation of inertial waves: A vector spectral analysis of velocity profiles. *Journal of Geophysical Research*, *80*(15), 1975–1978. https://doi.org/10.1029/JC080i015p01975

Lee, C. M., Cole, S., Doble, M., Freitag, L., Hwang, B., et al. (2012). Marginal Ice Zone (Miz) program: Science and experiment plan, Tech. Rep. APL-UW 1201, 48, Appl. Phys. Lab., University of Washington, Seattle, Washington.

Levine, M. D., Paulson, C. A., & Morison, J. H. (1985). Internal waves in the Arctic Ocean: Comparison with lower-latitude observations. *Journal of Physical Oceanography*, *15*(6), 800–809. https://doi.org/10.1175/1520-0485(1985)015<0800:IWITAO>2.0.CO;2

Lien, R. C., & Müller, P. (1992). Consistency relations for gravity and vertical modes in the ocean. *Deep Sea Research*, *39*(9), 1595–1612. https://doi.org/10.1016/0198-0149(92)90050-4

Lincoln, B. J., Rippeth, T. P., Lenn, Y.-D., Timmermans, M.-L., Williams, W. J., & Bacon, S. (2016). Wind-driven mixing at intermediate depths in an ice-free Arctic Ocean. *Geophysical Research Letters*, *43*, 9749–9756. https://doi.org/10.1002/2016GL070454

Martini, K. I., Simmons, H. L., Stoudt, C. A., & Hutchings, J. K. (2014). Near-inertial internal waves and sea ice in the Beaufort Sea. *Journal of Physical Oceanography*, *44*(8), 2212–2234. https://doi.org/10.1175/JPO-D-13-0160.1

McPhee, M. G. (1980). A study of oceanic boundary-layer characteristics including inertial oscillation at three drifting stations in the Arctic Ocean. *Journal of Physical Oceanography*, *10*(6), 870–884. https://doi.org/10.1175/1520-0485(1980)010<0870:ASOOBL>2.0.CO;2

McPhee, M. G. (2012). Advances in understanding ice-ocean stress during and since AIDJEX. *Cold Regions Science and Technology*, *76-77*, 24–36.

McPhee, M. G., & Kantha, L. H. (1989). Generation of internal waves by sea ice. *Journal of Geophysical Research*, *94*(C3), 3287–3302. https://doi.org/10.1029/JC094iC03p03287

Merrifield, M. A., & Pinkel, R. (1996). Inertial currents in the Beaufort Sea: Observations of response to wind and shear. *Journal of Geophysical Research*, *101*(C3), 6577–6590. https://doi.org/10.1029/95JC03625

Morison, J. H., Long, C. E., & Levine, M. D. (1985). Internal wave dissipation under sea ice. *Journal of Geophysical Research*, *90*(C6), 11,959–11,966. https://doi.org/10.1029/JC090iC06p11959

Peralta-Ferriz, C., & Woodgate, R. A. (2015). Seasonal and interannual variability of pan-Arctic surface mixed layer properties from 1979 to 2012 from hydrographic data, and the dominance of stratification for multiyear mixed layer depth shoaling. *Progress in Oceanography*, *134*, 19–53. https://doi.org/10.1016/j.pocean.2014.12.005

Pinkel, R. (2005). Near-inertial wave propagation in the western Arctic. *Journal of Physical Oceanography*, *35*(5), 645–665. https://doi.org/10.1175/JPO2715.1

Pinkel, R. (2008). The wavenumber-frequency spectrum of vertical and internal-wave shear in the Western Arctic Ocean. *Journal of Physical Oceanography*, *38*(2), 277–290. https://doi.org/10.1175/2006JPO3558.1

Rainville, L., & Windsor, P. (2008). Mixing across the Arctic Ocean: Microstructure observations during the Beringia 2005 expedition. *Geophysical Research Letters*, *35*, L08606. https://doi.org/10.1029/2008GL033532

Rainville, L., & Woodgate, R. A. (2009). Observations of internal wave generation in the seasonally ice-free Arctic. *Geophysical Research Letters*, *36*, L23604. https://doi.org/10.1029/2009GL041291

Randelhoff, A., Fer, I., & Sundfjord, A. (2017). Turbulent upper-ocean mixing affected by meltwater layers during Arctic summer. *Journal of Physical Oceanography*, *47*(4), 835–853. https://doi.org/10.1175/JPO-D-16-0200.1

Spreen, G., Kaleschke, L., & Heygster, G. (2008). Sea ice remote sensing using AMSR-E 89-GHz channels. *Journal of Geophysical Research*, *113*, C02S03. https://doi.org/10.1029/2005JC003384